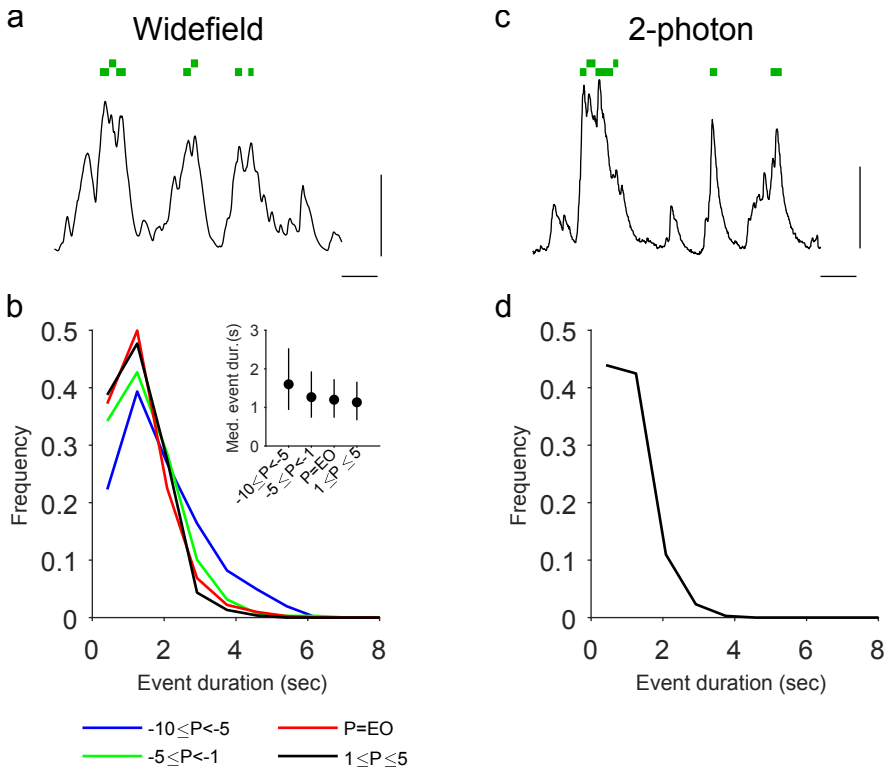

Extended Data Figure 1: Durations of spontaneous events. a. Timecourse of spontaneous activity (mean frame ΔF/F) measured during wide-field imaging. Green bars above trace indicate event epochs. Scale bars: 5 sec, 100% ΔF/F. **b**. Distribution of event durations across ages. *Inset*: Median and IQR of event duration across age. **c**. Timecourse of spontaneous activity measured at the single cell level with 2-photon imaging, plotted as mean ΔF/F across all cells. Green bars above trace indicate event epochs**.** Scale bars: 5 sec, 100% ΔF/F. **d**. Event durations measured at the cellular level are similar to those observed at a columnar scale with wide-field imaging.

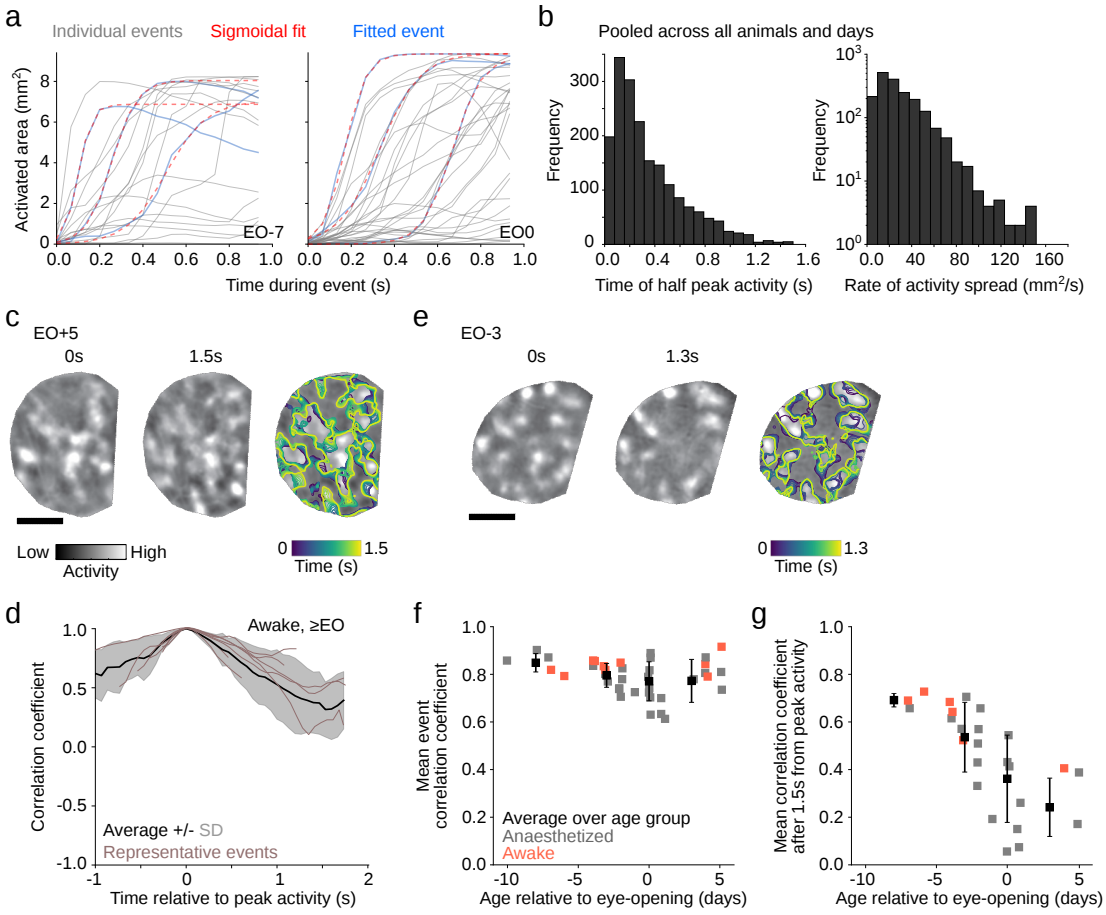

Extended Data Figure 2: Within events, the spatial pattern of spontaneous activity is fairly stable, in particular in the young. **a** Spread of activity during an event differs broadly across events. Activated cortical area (threshold=80% of total size of ROI) as a function of time from event onset for sets of representative events (gray lines). *Left*: from an animal 7 days prior to EO; *Right*: at EO. A sigmoidal function a/(1+exp(r(t-t_0)) was used to fit the traces. **b**, Distributions of time of half peak (t_0) and rate of activity spread (r*a/4). Rates >100mm²/s can hardly be distinguished from instantaneous/uniform rise of activity in our field of view. Events were pooled across all animals and all days. **c.** *Left*: Representative example of spontaneous activity during an event one day after eye-opening (EO). The spatial pattern changes moderately during the first 1.5 seconds (*left* and *middle*). *Right*: Contour lines delineating active regions across time (represented by color), superimposed on the frame at 1.5s. While there is moderate change, the basic layout is fairly stable. **d.** Pattern stability within individual events. Correlations of frames to frame at peak activity, for all awake animals post eye-opening (N=3). **e**. A representative example seven days prior to EO (as in a), showing a similar degree of stability across time. **f**. The mean correlation to peak, averaged across events for each animal, remains high and changes relatively little with age (12 individual animals). **g**. The average correlation coefficient 1.5s after the peak activity is decreasing during development being highest in the youngest animals. Age groups (black symbols) in **f** and **g** where EO-10 to EO-6, EO-5 to EO-1, EO, and >EO. Errorbars indicate SD across individuals. Only frames with activity above threshold (threshold=80% of total size of ROI) were considered. Scale bar is 1mm (c,e).

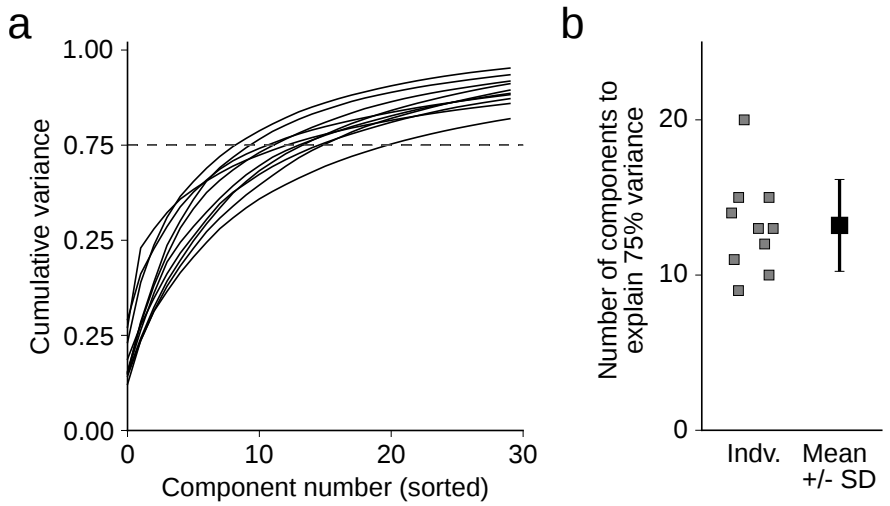

Extended Data Figure 3: Principal component analysis of spontaneous activity. a. The spontaneous activity events contain a moderate number of relevant principal components as shown by the cumulative explained variance. Gray dashed line indicates 75% variance. **b**. The number of components needed to explain 75% variance is shown for 10 individual animals (solid black) and the group mean ± SD (13±3, n=10 animals) is shown.

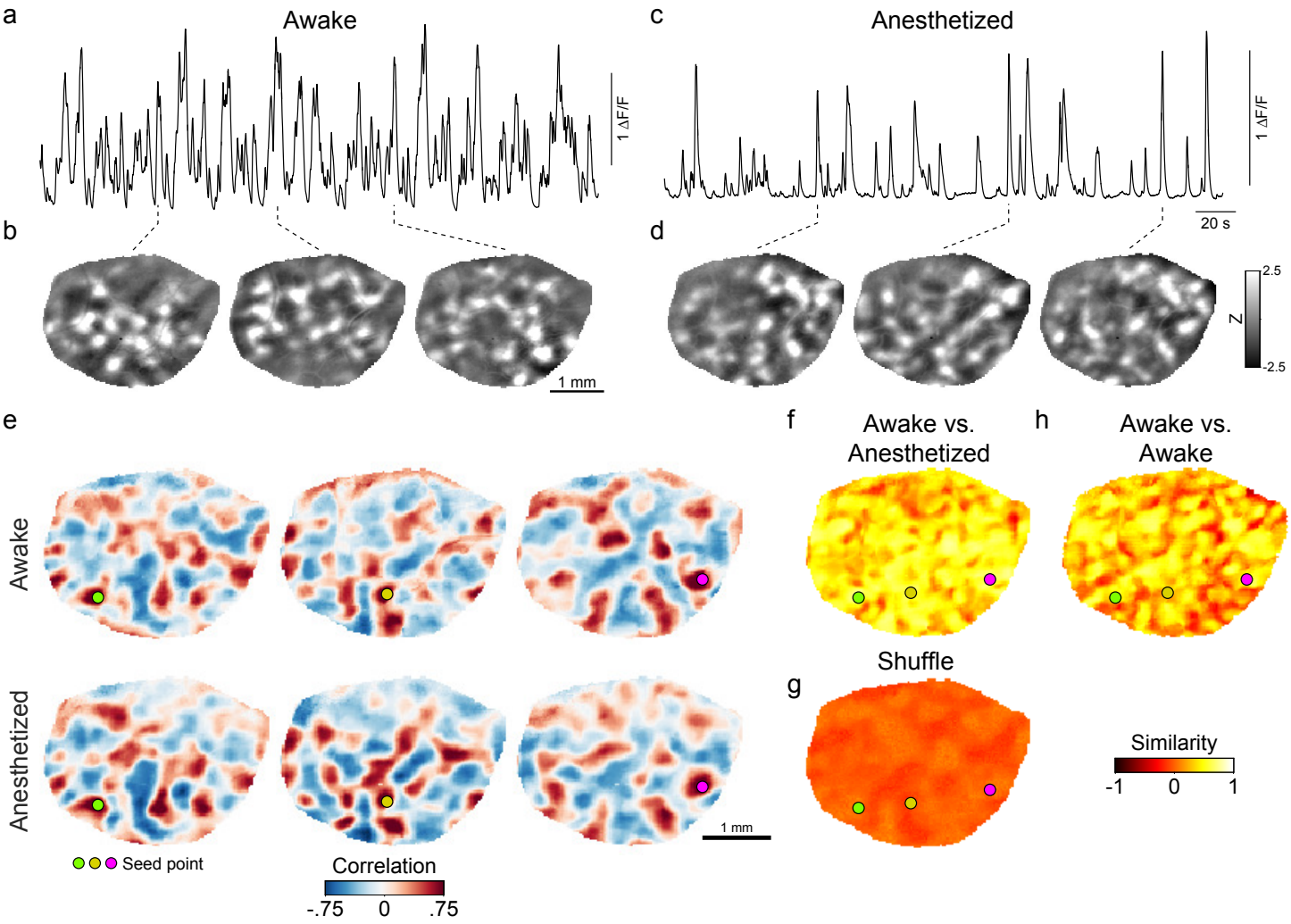

Extended Data Figure 4: Spatial structure of spontaneous correlations is not affected by anesthesia. a. Time course of spontaneous activity for awake animal (mean activity across ROI). **b**. Three representative events at times indicated. **c**. Time-course of spontaneous activity in same animal under anesthesia (0.5 – 1% isoflurane). **d**. Representative events. **e**. Three spontaneous activity correlation patterns for awake activity (top) and under anesthesia (bottom). **f**. Similarity of awake vs. anesthetized correlation patterns evaluated at each pixel in ROI. **g**. Similarity for shuffled patterns. **h**. Similarity of awake patterns calculated from 50% of spontaneous events to patterns calculated from remaining 50% of events.

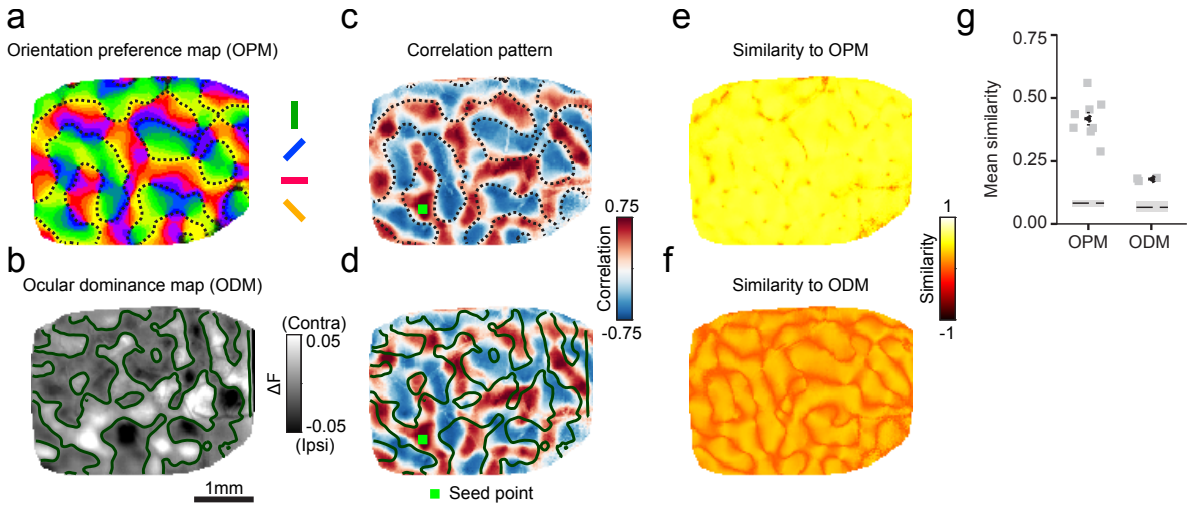

Extended Data Figure 5: The correlation structure of spontaneous activity more closely resembles the functional layout of iso-orientation domains than ocular dominance domains. a. An orientation preference map (OPM). The black-dotted line represents 0°-90° zero contours. **b.** An ocular dominance map (ODM). The dark green line represents zero-contours separating contralateral and ipsilateral domains. **c,d.** The contours from the OPM in (**c**) better match the correlation structure of spontaneous activity than the contours from the ODM in (**d**). The seed point in (**c**) and (**d**) corresponds to a region preferentially driven by a contralaterally presented horizontal grating. **e,f.** For the example animal shown in **a-d**, most spontaneous correlation patterns show higher similarity to the layout of the OPM (**e**) than to the ODM (**f**). **g.** On average, spontaneous correlation patterns show significantly higher pairwise similarity to the OPM than the ODM (p=0.02, Mann-Whitney U test, n=8 for orientation map and n=3 for ocular dominance map), but the mean pairwise similarity to both the orientation preference and ocular dominance maps is significantly higher than to control shuffled maps (p<0.0001, bootstrap test).

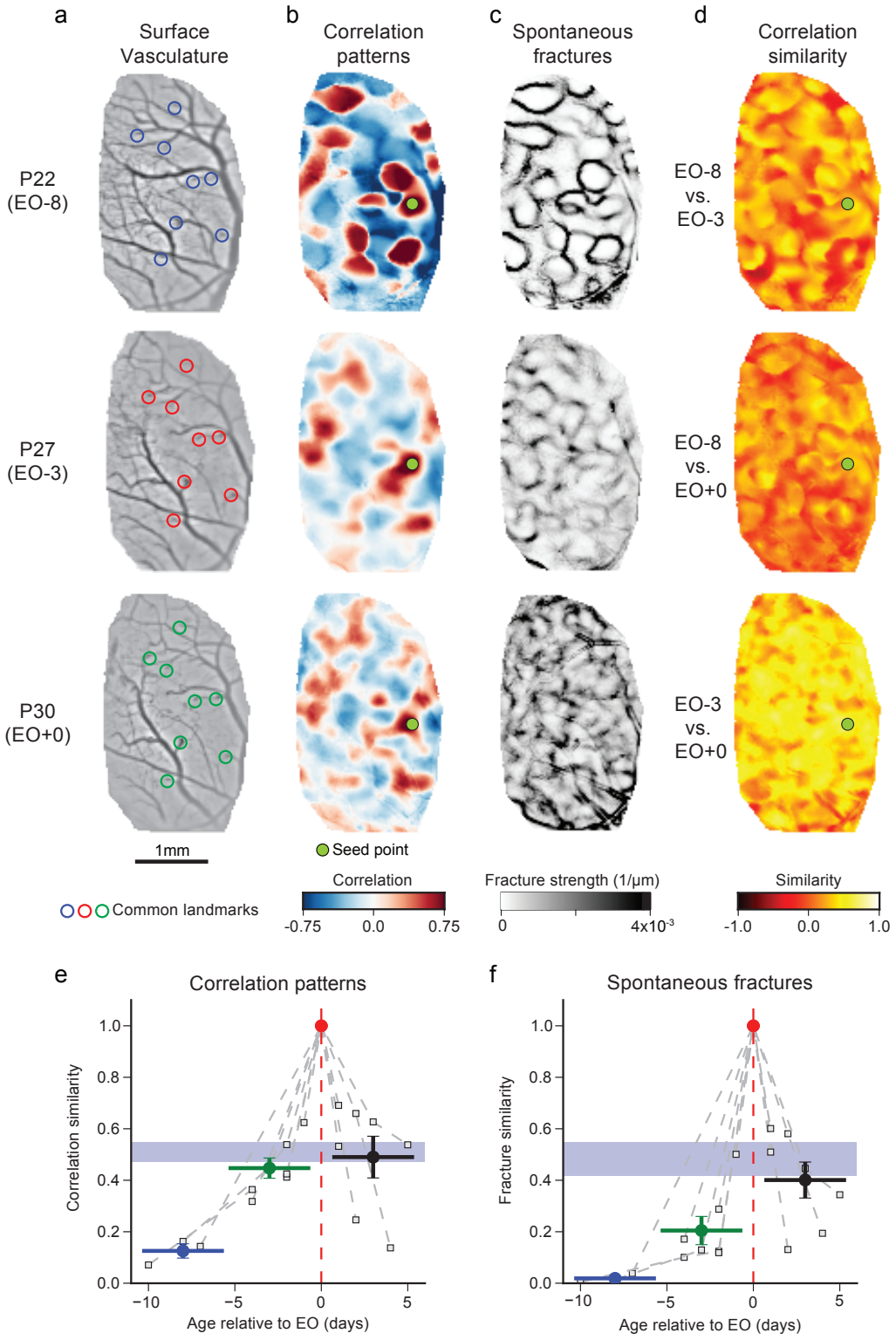

Extended Data Figure 6: Refinement of correlation structure during early development. a. Registration across days was achieved by matching radial (descending) blood vessels and computing an affine transform. **b**. Correlation patterns for same reference point over 8 days prior to eye opening. **c**. Spontaneous fractures. **d**. Similarity of correlation patterns to the next imaging session (*top*) or to final day (*middle and bottom*). **e**. Similarity of correlation patterns to reference day (eye opening; EO=0). Blue region indicates within-day similarity for subsampled reference day correlations. **f**. Similarity of spontaneous fracture patterns as a function of relative age.

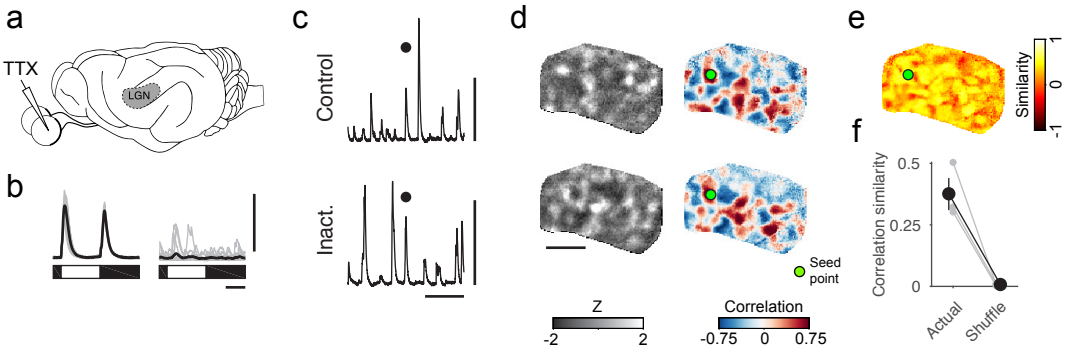

Extended Data Figure 7: Long-range correlations in spontaneous activity persist in the absence of retinal activity. a. Cortical spontaneous activity was measured before and following Retinal inactivation via intraocular injection of TTX. **b**. Cortical responses (averaged across all pixels in ROI) to full-field luminance changes before (*left*) and after (*right*) retinal inactivation. Scale bars: 5 sec, 0.5 ΔF/F. **c**. Time-course of spontaneous activity for mean of all pixels before (*top*) and after (*bottom*) inactivation. Scale bars: 30 sec, 0.15 ΔF/F. **d**. Representative spontaneous events (*left*) and correlation patterns (*right*) before (*top*) and after (*bottom*) inactivation. **e**. Similarity of correlation structure in representative experiment before and after inactivation for all cortical locations. (*top*) and versus shuffled data (*bottom*). Scale bar 1mm (d,e). **f**. The spatial structure of spontaneous events following LGN inactivation shows significantly more similarity across events.

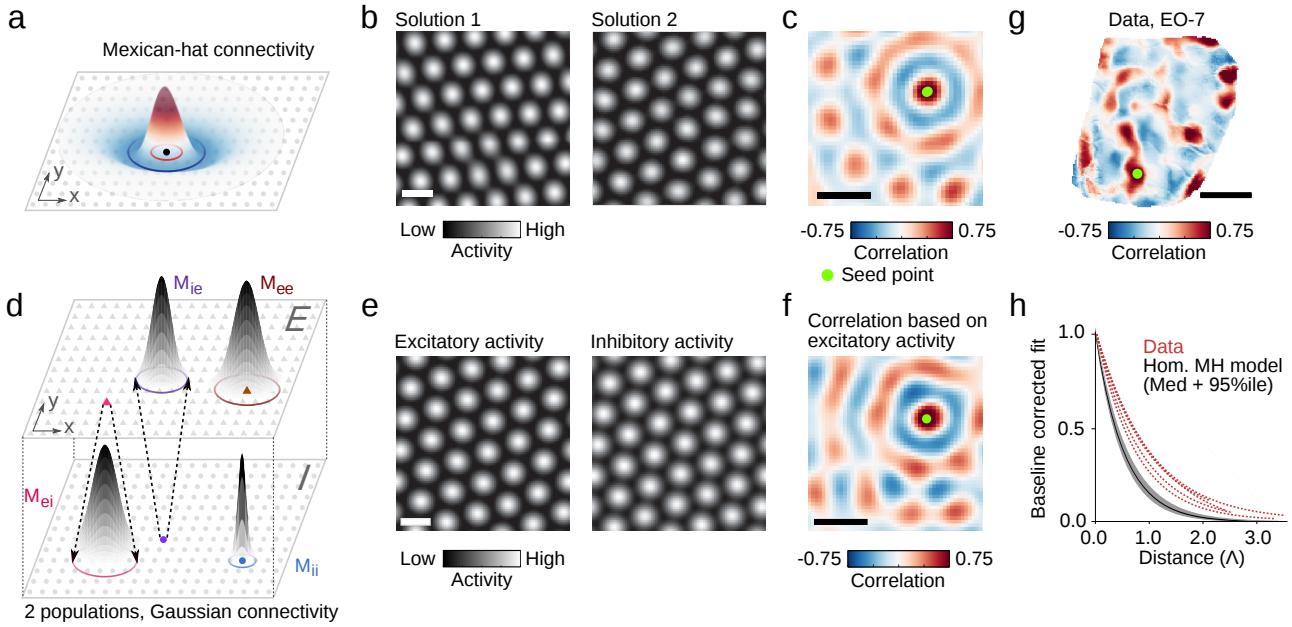

Extended Data Figure 8: Networks with homogeneous and isotropic connections generate modular and regular activity patterns, but do not account for the long-range correlations observed in early visual cortex. a. Model (i): The spatial profile of lateral connections follows an isotropic Mexican hat in all neurons. **b.** With constant input drive, the activity converges to a regular hexagonal patterns (two representative solutions are shown; simulations performed on a 100x100 grid, see Methods). **c.** Correlations between remote sites are only moderate, owing to the fact that all translated and rotated hexagonal patterns are solutions as well (computed over 100 solutions). **d.** Model (ii): An excitatory (E) and inhibitory (I) population. Connections within E and from E to I both follow the same isotropic Gaussian profile. Connections from I also follow Gaussian profiles, but have a shorter spatial range. **e**, Representative solution of excitatory (*left*) and inhibitory (*right*) population (parameter setting: a_{ee} = 22.2, a_{ei}=a_{ie}=21.6, a_{ii}=20.8, σ_e=*1.9* σ_{ei} = 1.4, σ_{ii}=*0.6*); simulations performed on a 80x80 grid, see Methods). **f.** Correlation pattern (as in c) for the excitatory population. **g.** Representative example of a correlation pattern observed in ferret visual cortex 7 days prior to eye-opening. **h.** For the correlation patterns in the early cortex the peak values decay significantly slower with spatial distance from the seed points (fits, dashed red; N=5) than in model (i) (**a**) (104 patterns, p<0.0097), model (ii) (**d**) (109 patterns, p<0.009) and in an ensemble of randomly shifted and rotated ideal hexagonal patterns (100 patterns, p<0.01). To assess significance we used bootstrap tests for all three comparisons, see Methods. All correlations were baseline corrected, see Methods. Scale bars: domain spacing 1Λ (b, c, f, g); 1mm (h).

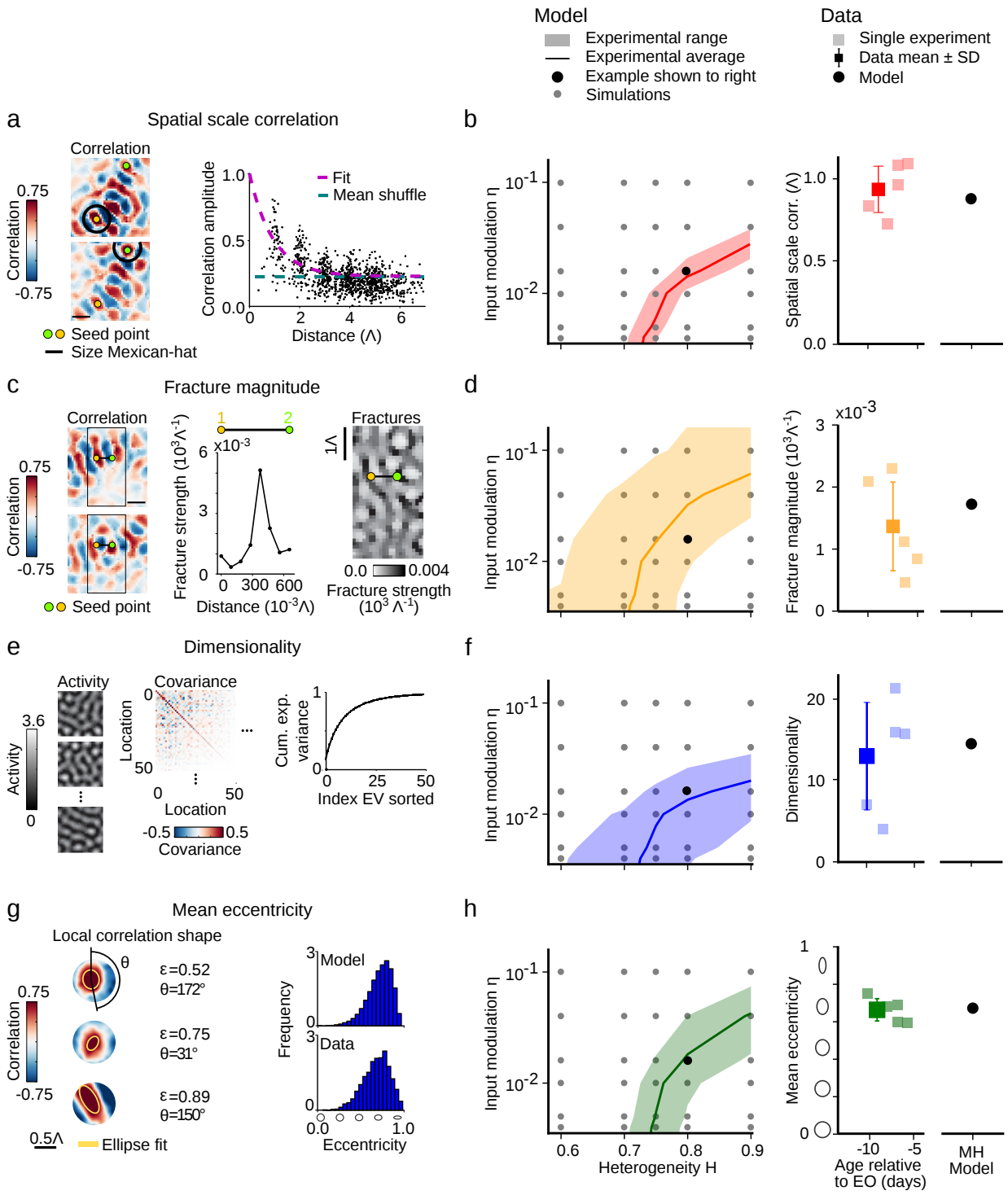

Extended Data Figure 9: Comparison of early *in vivo* spontaneous data to dynamical model. **a**, **c**, **e**, **g**: Model analysis; **b**, **d**, **f, h**: Comparison model vs. experiment. **a.** Long-range organization of correlation patterns (*left*) is quantified by fitting an exponential decay to the peaks (local maxima) in the correlation pattern as a function of their distance to the seed point, using all correlation patterns. **b.** *Left:* Shaded region in the diagram with systematically varied heterogeneity and input modulation indicates the parameter settings in which the model values for correlation pattern scale lie within the interval (mean ± SD) given by the experimental data (n=4 animals, 5 experiments). The parameter setting of the example shown in Fig. 4j (red triangle in 4j) is highlighted. *Right:* Comparison of dimensionality for indicated model parameters and experimental data. **c.** The geometrical layout of correlation patterns (*left*) can change drastically over only a short distance (*middle*). Rate of change reveals organization of fractures (*right*). Region of fractures shown is highlighted by black box in correlation patterns (*left*). **d**. Comparison of fracture magnitude with experimental data. **e.** Covariance matrix (*middle*) over 100 spontaneous activity events (*left*) shows that different locations co-vary. A moderate number of components (*right*) is needed to explain 75% of the variance indicating low dimensional activity patterns. **f.** Comparison of dimensionality for model with experimental data. **g.** *Left*: The anisotropic structure of local correlation (i.e. the peak around the seed point) is quantified by fitting an ellipse to the 0.7 contour line (least-square fit) and computing its eccentricity. *Right:* The eccentricity of local correlation shows a similar distribution in data and model. **h**. Comparison of eccentricity of local correlation with experimental data.

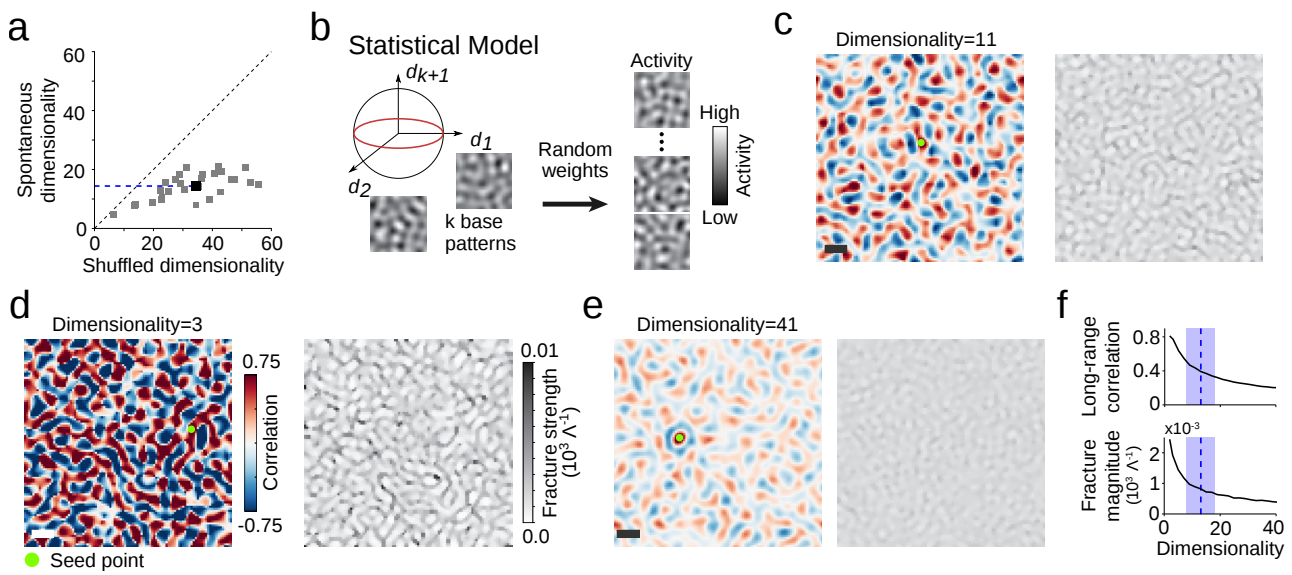

Extended Data Figure 10: Constraining activity patterns to low dimensionality can generate long-range correlations and pronounced fractures. a Spontaneous activity patterns are significantly lower-dimensional than shuffled controls. **b** A statistical model generates pattern ensembles with dimensionality *k* by superposition of *k* orthonormal basis patterns with random weights. The correlation pattern computed over an ensemble of n=10000 patterns and dimensionality *d*=11 expresses long-range correlations (**c**, *left*) and pronounced fractures (**c**, *right*). Example spontaneous correlation pattern (*left*) and fractures (*right*) for dimensionality *d* = 3 (**d**), and *d* = 41 (**e**). **f** The strength of long-range correlations and fractures both increase with decreasing dimensionality. Blue lines (mean +/- SD) indicate the range of dimensionality in the data (**a**). Scale bar is 1Λ.

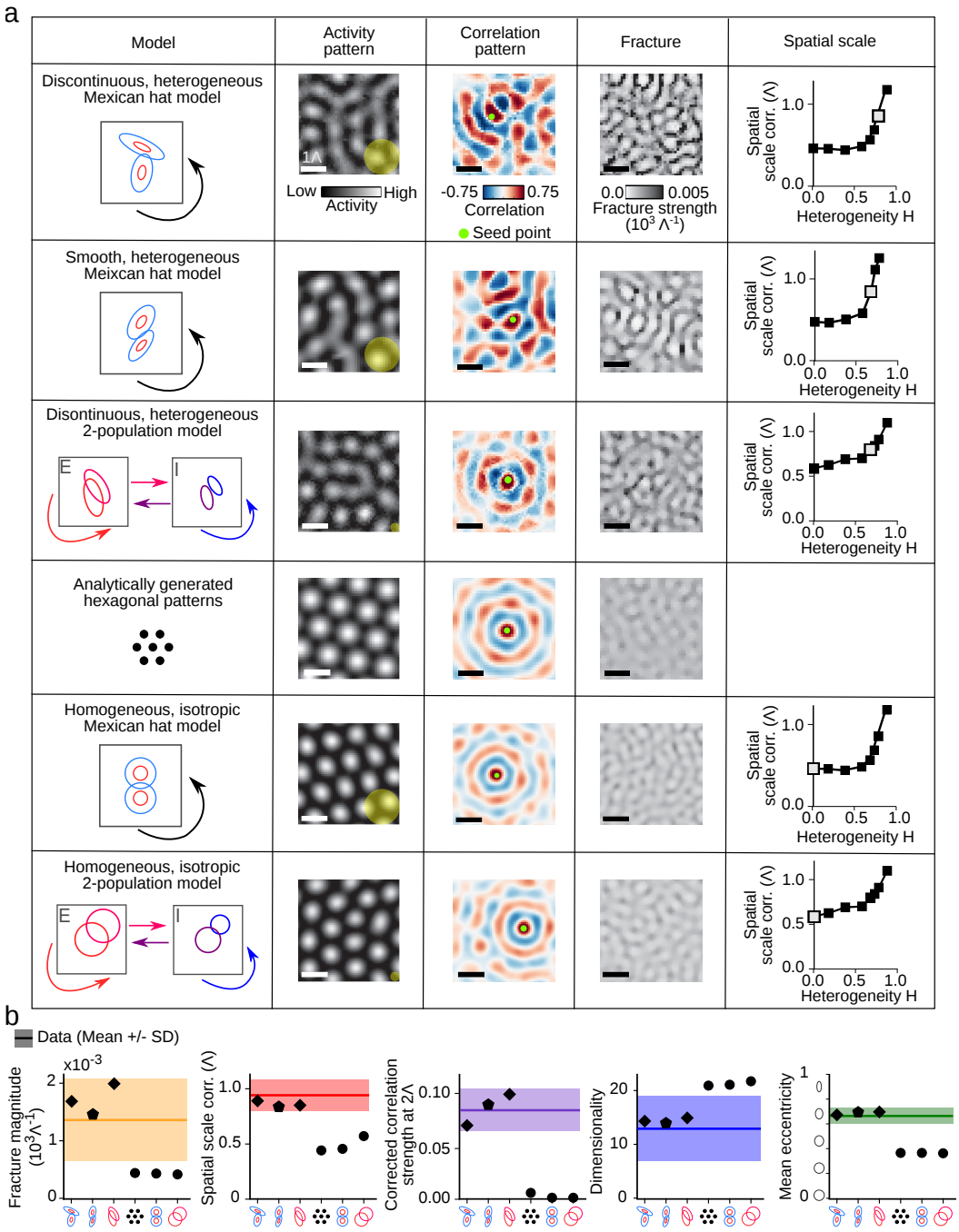

Extended Data Figure 11: Systematic overview over different variants of the two types of circuit models studied, showing the correlation structure they produce. a, Columns (left to right): schematic diagram of model, a typical activity pattern, a representative correlation pattern, correlation fractures, and the spatial scale of correlations for the value of heterogeneity of connections, H, used (open symbol) and for varying H (closed symbols). The yellow circle on top of the activity patterns indicates the size of the average local connectivity. Rows (top to bottom): (1) The model shown in Fig. 4 (Mexican hat connectivity, H=0.8, η=0.016). (2) As in (1), but here the properties of the Mexican hat vary smoothly across space, on a spatial scale Λ marked by the scale bar on the activity pattern. Results are similar to the discontinuous version (1). (3) The model with two separate populations for inhibitory and excitatory neurons in the discontinuous, heterogeneous regime, analogue to (1) (H=0.7, η=0.01). In the heterogeneous regime, all three models (1-3) agree quantitatively with experiment. (4) Ideal hexagonal patterns, sampled from the distribution known to be the solution set for isotropic, homogeneous Mexican hat connectivity. Rows (5) and (6): Numerical solutions of the isotropic homogeneous versions of models (1) and (3) respectively. For (4)-(6) the correlation structure is inconsistent with experiment. The yellow circle on top of the activity patterns indicates the size of the average local connectivity (MH models only). All scalebars are 1Λ. **b**, Quantitative comparison of models (1) to (6) with experiment. Shown are (from left to right; mean (solid line) +/- SD (shaded region)): the fracture strength, the spatial scale, the average at correlation peaks at 2Λ subtracted by the shuffle average correlation, the dimensionality, and the mean eccentricity (see Methods). The heterogeneous network models all lie within the experimentally observed range of values for all five quantities, while this is not the case for models with homogenous, isotropic connectivity.

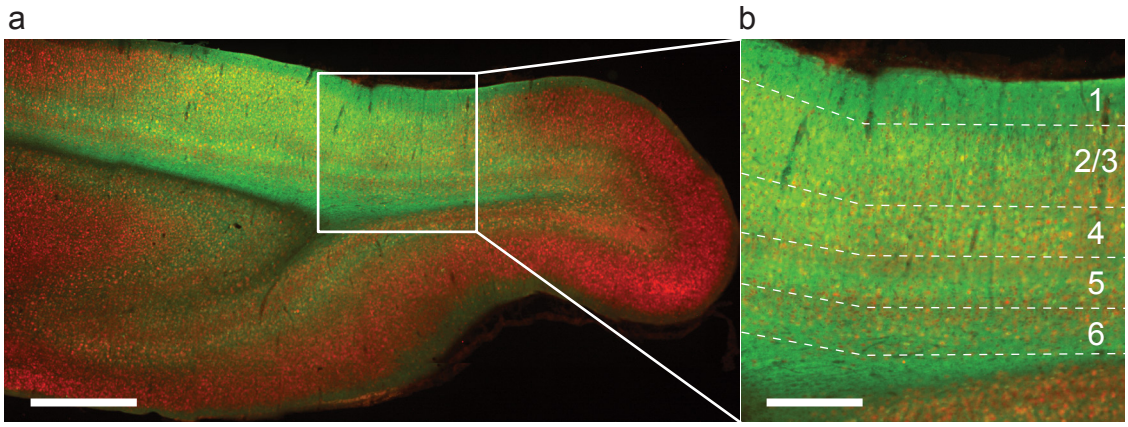

Extended Data Figure 12: Virally-mediated labelling of visual cortex with GCaMP6s. a. Coronal section showing widespread GCAMP6 expression in layer 2/3 neurons of primary visual cortex (Green - GCAMP6s / Red - NeuN). **b**. Expanded view of region indicated in (**a**). Scale bars are 1 mm (**a**) and 0.5 mm (**b**).

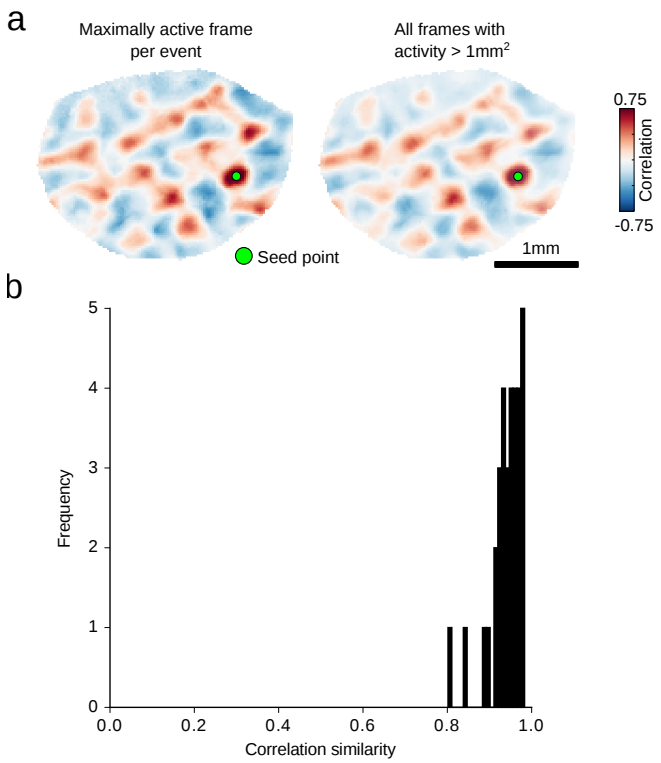

Extended Data Figure 13: Correlation patterns from all events are highly similar to those computed from large events only. a. Example correlation pattern calculated over only the maximally active frames of large events (*left*) is highly similar to correlation pattern from same seed point calculated over all frames of all events (*right*). **b.** The average similarity between all correlation patterns within the ROI are shown for n=12 animals, n=33 experiments throughout development.

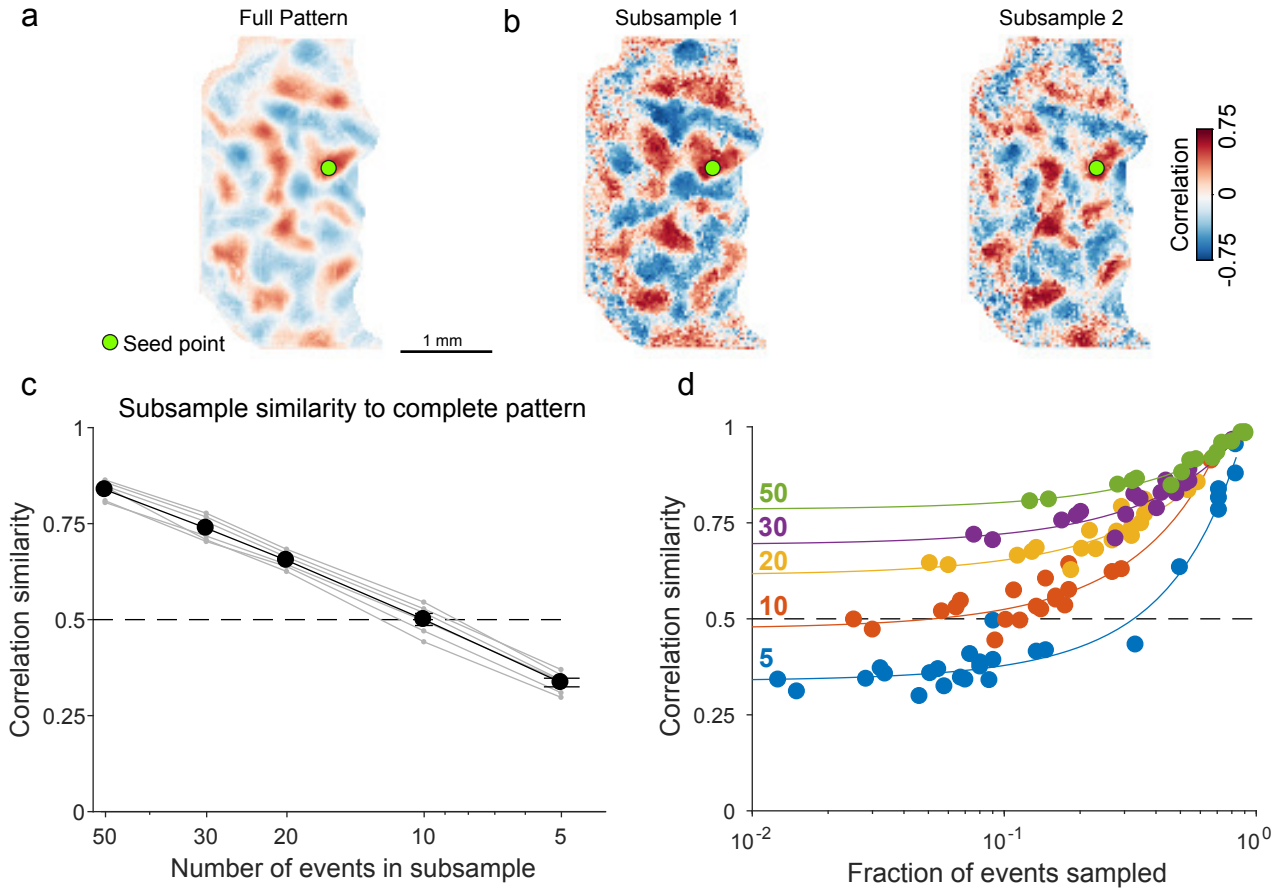

Extended Data Figure 14: Minimum number of spontaneous events required to estimate correlations. a. Correlation pattern from all events (393 events) for a seed point indicated in green. **b.** Two example correlation patterns produced by randomly subsampling 10 of 393 events. **c**. Similarity (second order correlation) of subsampled correlation patterns to the pattern computed from all events (n=6 experiments with >100 spontaneous events). Correlation similarity of 0.5 is reached with approximately 10 events. Gray marker indicate individual animals, black marker indicate mean. **d**. Similarity of subsampled correlation patterns to complete pattern as a function of the fraction of events sampled for 5, 10, 20, 30, or 50 events (blue, orange, yellow, purple, and green curves respectively). Subsamples of 10 events asymptote at a similarity of approximately 0.5, even for cases with a large number of events (in which the fraction of events sampled is very low), indicating that 10 events is sufficient to capture major features of correlation structure.

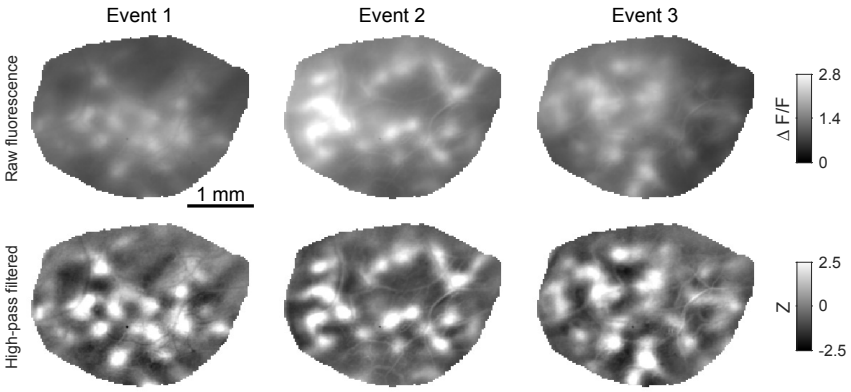

Extended Data Figure 15: Spatial high-pass filtering of modular spontaneous activity. Representative spontaneous events shown as ΔF/F (*top*) and after high-pass filtering (*bottom*). Modular nature of spontaneous events is clearly evident already prior to filtering.

Animal	Fig. 1a-h; Ex Fig. 4	Fig. 1i; Ex Fig. 1c-d	Fig. 1 in-text stats (event rate; duration; correlation strength at 2mm); Ex Fig. 3	Ex Fig. 1a-b; Fig. 3d-e; Ex Fig. 10	Ex Fig. 2	Fig. 2	Ex Fig. 5	Fig. 3a-c	Fig. 3g-h; Ex Fig. 6e-f
F1579			32 (1)	31 (0); 32 (1)	31 (0); 32 (1)				31 (0); 32 (1)
F1581			32 (1)	30 (-1); 31 (0); 32 (1)	30 (-1); 31 (0); 32 (1)				30 (-1); 31 (0); 32 (1)
F1642					31 (-2); 33 (0); 36 (3); 38 (5)	38 (5)	38 (5) - OR/OD		31 (-2); 33 (0); 36 (3); 38 (5)
F1664			30 (0)	23 (-7); 30 (0)	23 (-7); 30 (0)			**23 (-7)**	23 (-7); 30 (0)
F1665			31 (0)	21 (-10); 27 (-4); 29 (-2); 31 (0)	21 (-10); 27 (-4); 29 (-2); 31 (0)				**21 (-10); 27 (-4); 29 (-2); 31 (0)**
F1666			30 (0)	22 (-8); 27 (-3); 30 (0)	22 (-8); 27 (-3); 30 (0)				22 (-8); 27 (-3); 30 (0)
F1667					26 (-2); 28 (0)				
F1768			35 (0)	31+ (-4); 35 (0)	31+ (-4); 35 (0)				31+ (-4); 35 (0)
F1770			35 (1)	27+ (-7); 28+ (-6); 31+ (-3); 35 (1)	27+ (-7); 28+ (-6); 31+ (-3); 35 (1)				27+ (-7); 28+ (-6); 31+ (-3); 35 (1)
F1784	37^ (5)	30* (-2)	37* (5)	30* (-2); 37* (5)	30* (-2); 37* (5)	**37* (5)**			30* (-2); 37* (5)
F1785	**30^ (-2)**; 36^ (4)	**30* (-2)**; 36* (4)	36* (4)	28+ (-4); **30* (-2)**; 36* (4)	28+ (-4); 30* (-2); 36* (4)				28+ (-4); 30* (-2); 36* (4)
F1786	28^ (-3); 35^ (4)	28* (-3); 35* (4)	35* (4)	28* (-3); 35* (4)	**28* (-3); 35* (4)**				28* (-3); 35* (4)
F1492						39 (9)	39 (9) - OR		
F1509						37 (5)	37 (5) - OR		
F1532						39 (7)	39 (7) - OR		
F1643						37 (5)	37 (5) - OR/OD		
F1654						47 (12)	47 (12) - OR		
F1655						43 (16)	**43 (16) - OR/OD**		
F2122									
F2124									
F2125									
F1953									
F1954									
F1957									

Animal	Ex Fig. 6a-d	Fig. 4a-g	Ex Fig. 7	Ex Fig. 8h,i Ex Fig. 9	Ex Fig. 13	Ex Fig. 14	Ex Fig. 15	Ex Movie 1-4	Ex Movie 5
F1579					31 (0); 32 (1)	31 (0); 32 (1)			
F1581					30 (-1); 31 (0); 32 (1)	30 (-1); 31 (0); 32 (1)			
F1642					31 (-2); 33 (0); 36 (3); 38 (5)	31 (-2); 33 (0); 36 (3); **38 (5)**			
F1664				**23 (-7)**	23 (-7); 30 (0)	23 (-7); 30 (0)			**23 (-7)**
F1665				21 (-10)	21 (-10); 27 (-4); 29 (-2); 31 (0)	21 (-10); 27 (-4); 29 (-2); 31 (0)			
F1666	**22 (-8); 27 (-3); 30 (0)**			22 (-8)	22 (-8); 27 (-3); 30 (0)	22 (-8); 27 (-3); 30 (0)			
F1667					26 (-2); 28 (0)	26 (-2); 28 (0)			
F1768					31+ (-4); 35 (0)				
F1770				27+ (-7); 28+ (-6)	27+ (-7); 28+ (-6); 31+ (-3); 35 (1)				
F1784					30* (-2); 37* (5)				
F1785					28+ (-4); **30* (-2)**; 36* (4)		**30* (-2)**	**30+^* (-2)**	
F1786					28* (-3); 35* (4)				
F1492									
F1509									
F1532									
F1643									
F1654									
F1655									
F2122		25 (?)							
F2124		**24 (?)**							
F2125		22 (?)							
F1953			27 (?)						
F1954			**29 (?)**						
F1957			24 (?)						

Numbers indicate Age (EO) at time of experiment.
Example experiments are highlighted in yellow and bold text.
EO is unknown for acute imaging experiments performed prior to eye opening and is indicated by (?)

+ indicates awake activity
^ indicates comparison of awake and anesthetized activity
* indicates pooling awake and anesthetized activity

Extended Data Table 1: List of experiments used in analysis.

Extended data movie 1: Spontaneous activity in the awake visual cortex is highly dynamic and modular. Ongoing spontaneous activity visualized through wide-field calcium imaging shows highly dynamic distributed sets of active domains spanning millimeters. This approach affords high signal-to-noise measurements of large-scale spontaneous activity, with active domains clearly visible. Spontaneous activity was recorded in a dark room, while viewing a black screen. Trace shows activity (ΔF/F) for a single pixel located at center of blue box. Green bars above trace indicate event epochs, with red dots indicating the maximally-active frame for each event used to compute correlations. Movie frames are raw fluorescence images. Movie is shown in real time, scale bar: 1mm.

Extended data movie 2: Spontaneous correlation patterns are highly diverse and show both fine- and large-scale organization across the cortical surface. Moving the correlation seed point across the cortical surface reveals a broad range of correlation patterns, indicating the presence of multiple distributed functional networks within the visual cortex. Across most of the cortical surface, large-scale correlation patterns change smoothly, however this progression is occasionally punctuated by abrupt shifts in correlation structure between nearby seed points, revealing the fine-scale precision of distributed functional networks. Scale bar: 1mm.

Extended data movie 3: Spontaneous activity in the anesthetized visual cortex shows large-scale modular activity patterns. Raw fluorescence images showing spontaneous activity in the same ferret as Extended Data Movie 1 under isoflurane anesthesia (0.5-1%), during viewing of a black screen. Movie is shown in real time, scale bar: 1mm. Trace shows activity (ΔF/F) for a single pixel located at center of blue box. Green bars above trace indicate event epochs, with red dots indicating the maximally-active frame for each event used to compute correlations.

Extended data movie 4: Spontaneous activity at the cellular level is modular and locally coherent. 2-photon imaging of spontaneous activity in the awake ferret cortex during viewing of black screen shows adjacent regions of co-active neurons. Images are shown as raw fluorescence, temporally smoothed with a 167 ms median filter. Movie is shown in real time, scale bar: 200μm. Trace shows mean population activity (ΔF/F) for all cells in FOV. Green bars above trace indicate event epochs used to compute correlations.

Extended data movie 5: Spontaneous activity in the early visual cortex shows widespread modular activity patterns. Spontaneous activity in ferret visual cortex imaged at P23 under isoflurane anesthesia (0.5-1%) during viewing of black screen. Images are shown as $\Delta F/F_0$, clipped to 0-150%. Movie is shown in real time, scale bar: 1mm.

Extended Data Supplementary Notes (Smith et al., Long-range order from local interactions: organization and development of distributed cortical networks.)

Long-range correlations from short-range connections without Mexican hat profile
In the main text, we show that lateral connections that are short-range but heterogeneous can produce activity patterns that are correlated over an extended distance in space (Fig. 4h-l). This mechanism provides a potential explanation for the long-range correlations we observe in early ferret visual cortex at a time before long-range anatomical connections form. In our model the lateral connections are assumed to support the formation of active domains, reflecting our observation that spontaneous activity in the early visual cortex is always modular. The dynamical mechanism we assume for generating modular patterns of activity is known as the Turing-mechanism [44]: modular patterns arise from a spatially homogeneous state by amplifying spatially heterogeneous perturbations through dynamical feedback loops mediated by the recurrent connections [45].

Since the focus of our study lies on the mechanisms causing active modules to be correlated over larger distances, we chose a generic local circuit motive known to implement the Turing-mechanism, the so-called Mexican hat connectivity (local excitation with lateral inhibition). Although there is evidence for such a motif from studies using glutamate uncaging in slices of ferret visual cortex at developmental stage similar to those we examine [46,47], other studies using paired recordings in slices of adult rat cortex [48], suggest that in fact the spatial range of inhibition is smaller than the range of excitation. This raises two important questions, to be addressed in the following. First, can lateral connections without a Mexican hat profile, i.e. with inhibition that is more short-range than excitation, produce modular patterns of activity? Second, would in this case heterogeneity in the lateral connections induce long-range correlations, as it does in the model based on Mexican hat connectivity, which is studied in Fig. 4?

In the following, we first describe a network model that produces modular activity patterns from local connections that do not exhibit a Mexican hat profile, building on previous work [49,50]. The model consists of an excitatory and an inhibitory neural population and neurons are linked via local lateral connections (with Gaussian profiles). We consider a regime, in which the range of connections formed by excitatory neurons is more than 30% larger than that of inhibitory neurons. We show that this model produces activity patterns very similar to those obtained in the one-population model with Mexican hat connectivity in Fig. 4.

In a second step, we ask whether this two-population model can produce long-range network correlations, despite its only local lateral connections. We find that it can indeed account quantitatively for all aspects of the spontaneous activity correlation structure that we observe in the early visual cortex. It does so when the connectivity is sufficiently heterogeneous across space, i.e. when the connectivity parameters vary considerably across neurons, analogous to the heterogeneity assumed in the one-population model in Fig. 4. Both models produce very similar results, indicating that the effect of heterogeneity is largely independent from the specific form of network interactions generating modular activity.

Modular activity through lateral connections without Mexican hat profile
Spontaneous activity in the early visual cortex is modelled by the following dynamics:

$$\tau \frac{du_e(\mathbf{x},t)}{dt} = -u_e(\mathbf{x},t) + \left[\gamma \sum_{\mathbf{y}} \left(M_{ee}(\mathbf{x},\mathbf{y})u_e(\mathbf{y},t) - M_{ei}(\mathbf{x},\mathbf{y})u_i(\mathbf{y},t)\right) + J_e(\mathbf{x})\right]_+ , \tag{S1}$$

$$\tau \frac{du_i(\mathbf{x},t)}{dt} = -u_i(\mathbf{x},t) + \left[\gamma \sum_{\mathbf{y}} \left(M_{ie}(\mathbf{x},\mathbf{y})u_e(\mathbf{y},t) - M_{ii}(\mathbf{x},\mathbf{y})u_i(\mathbf{y},t)\right) + J_i(\mathbf{x})\right]_+ , \tag{S2}$$

$$\text{with} \quad [x]_+ = \begin{cases} x & \text{if} \quad x > 0 \\ 0 & \text{else} \end{cases} \tag{S3}$$

where $u_e(x,t)$ ($u_i(x,t)$) is the average firing rate of an excitatory (inhibitory) unit at location $\boldsymbol{x}$ in a two-dimensional model cortex. τ is the neuronal time constant and assumed to be the same for excitatory and inhibitory units. $M_{mn}(\boldsymbol{x},\boldsymbol{y})$ are the synaptic weights connecting location $\boldsymbol{y}$ in population n to location $\boldsymbol{x}$ in population m ($m,n \in \{e,i\}$, with e being the excitatory and i the inhibitory population). The sum goes over all locations $\boldsymbol{y}$ within the network. γ is a factor controlling the overall strength of synaptic weights. Both excitatory and inhibitory units cover space uniformly and with equal density. $J_m(\boldsymbol{x})$ is the input to location $\boldsymbol{x}$ in population m.

The connectivity matrix m consists of the four synaptic weight matrices $M_{mn}(\boldsymbol{x},\boldsymbol{y})$ that are assumed to be short-range and modelled by isotropic Gaussians:

$$M(\mathbf{x},\mathbf{y}) = \begin{pmatrix} M_{ee}(\mathbf{x},\mathbf{y}) & -M_{ei}(\mathbf{x},\mathbf{y}) \\ M_{ie}(\mathbf{x},\mathbf{y}) & -M_{ii}(\mathbf{x},\mathbf{y}) \end{pmatrix}, \tag{S4}$$

$$M_{mn}(\mathbf{x},\mathbf{y}) = M_{mn}(|\mathbf{x}-\mathbf{y}|) = \frac{a_{mn}}{2\pi\sigma_{mn}^2} \exp\left(-\frac{|\mathbf{x}-\mathbf{y}|^2}{2\sigma_{mn}^2}\right) \tag{S5}$$

$$m, n \in \{e, i\}.$$

Here σ_{mn} denotes the SD and a_{mn} the strength of the Gaussian that connects population n to m. The a_{mn} were normalized such that the maximal eigenvalue of m is equal to 1. Note that the Gaussian connectivity profile is isotropic and identical for all units. Thus, the network connectivity exhibits rotation and translation symmetry.

To model a spontaneous event, we assumed an input drive constant in time and space with a value $J_e(\boldsymbol{x}) = J_i(\boldsymbol{x}) = J = 1$. We set τ=1, γ=1.02 and used random initial conditions $u_e(\boldsymbol{x},t=0)$, $u_i(\boldsymbol{x},t=0)$ drawn from a Gaussian distribution with zero mean and unit SD rectified at zero. The parameters for the connectivity were set to a_{ee}=22.2, a_{ie}=a_{ei}=21.6, a_{ii}=20.8, σ_{ee}=σ_{ie}=1.9, σ_{ei}=1.4, σ_{ii}=0.6. (Changing these values by 10% produced qualitatively similar results.) We integrated the network dynamics until a near steady state of the dynamics was reached. The results in Extended Data Figs. 8f, 11 were obtained for an integration time of 500τ. Different spontaneous events were obtained by using different initial conditions (same connectivity m and input J). We numerically integrated the dynamics using a 4th order Runge-Kutta method in a square region of size 80 x 80 using periodic boundary conditions and a time step dt=0.15τ. The simulations were performed on the GPUs

GeForce GTX TITAN Black and GeForce GTX TITAN X. The code was implemented in Python and Theano (version 0.8.1).

The activity patterns produced by this model were modular and exhibited a regular, hexagonal structure, similar to the solutions obtained for the simpler model with isotropic Mexican hat connectivity [45,51] studied in Fig. 4 (compare Extended Data Fig. 8, b and e). The active modules for the excitatory population showed a similar orientation and phase as those of the inhibitory population (Extended Data Fig. 8, e). Different solutions (obtained using different initial conditions) consisted of translated and rotated versions of the same hexagonal pattern, reflecting the symmetries of the model equations. The formation of hexagonal patterns is typical for two-dimensional systems with Turing instability characterized by translation and rotation symmetry and a broken z-symmetry (here the activity u) [52]. In our numerical simulations, hexagonal activity patterns occurred for a broad range of connectivity parameters. In other regimes, we also observed uniform or oscillatory solutions, to be characterized in detail elsewhere (manuscript in preparation). Thus, we conclude that lateral connections can produce modular patterns of activity, even if inhibition extends over a shorter range than excitation.

Heterogeneity in the connections induces long-range correlations consistent with the experimental data

Importantly, the correlation structure for an ensemble of solutions of the model described above decays on a significantly shorter range, when compared to size-matched sets of activity patterns measured in the early visual cortex (Extended Data Fig. 8h). The reason for this is that the ensemble of patterns this model produces reflects the symmetries of the underlying dynamics and thus consists of all translated and rotated versions of a hexagonal pattern. The same applies to the one-population model with Mexican hat connectivity (Extended Data Fig. 8a) and also to an ideal hexagonal ensemble, synthesized by applying (uniformly distributed) random translations and rotations to a solution of the model (Extended Data Fig. 8h). Thus, while both models can account for the fact that spontaneous activity is modular, their correlation structure is inconsistent with our experimental data (Extended Data Figs. 8h, 11b).

Therefore, we next ask whether introducing heterogeneity in the two-population model above (eqs.. (S1) and (S2)) induces correlations that are long-range, as in the case of the one-population Mexican hat model in Fig. 4h-l. As before, we introduce heterogeneity by making the Gaussian connectivity matrices M_{mn} anisotropic and by varying the strength of elongation, and the orientation and size of its axis across space (discontinuously, as in the one-population Mexican hat model):

$$M(\mathbf{x},\mathbf{y}) = \begin{pmatrix} M_{ee}(\mathbf{x},\mathbf{y}) & -M_{ei}(\mathbf{x},\mathbf{y}) \\ M_{ie}(\mathbf{x},\mathbf{y}) & -M_{ii}(\mathbf{x},\mathbf{y}) \end{pmatrix}, \tag{S6}$$

$$M_{mn}(\mathbf{x},\mathbf{y}) = \frac{a_{mn}}{2\pi\sigma^1_{mn}\sigma^2_{mn}} \exp\left(-\frac{1}{2}(R(\mathbf{x}-\mathbf{y}))^T\Sigma^{-1}_{mn}R(\mathbf{x}-\mathbf{y})\right), \tag{S7}$$

$$\text{with} \quad \Sigma_{mn} = \begin{pmatrix} (\sigma^1_{mn})^2 & 0 \\ 0 & (\sigma^2_{mn})^2 \end{pmatrix}, \tag{S8}$$

$$R = \begin{pmatrix} \cos(\phi) & -\sin(\phi) \\ \sin(\phi) & \cos(\phi) \end{pmatrix}, \tag{S9}$$

$$m,n \in \{e,i\}.$$

Here, $M_{mn}(\boldsymbol{x},\boldsymbol{y})$ is the connectivity from location $\boldsymbol{y}$ in population n to location $\boldsymbol{x}$ in population m. The quantities $\sigma_{mn}{}^1$ and $\sigma_{mn}{}^2$ denote the SD of the Gaussian in the direction of its major and minor axis, respectively. The angle φ determines the orientation of the elongated Gaussian. The dependence of these parameters on cortical space $\boldsymbol{x}$ is suppressed for clarity. a_{mn} denotes the connectivity strength.

To study systematically the effect of heterogeneity, we define a heterogeneity parameter H and use eccentricity ε to measure the degree of elongation of the Gaussians, as before (see Methods Eq. (11)). To construct a network, at each location $\boldsymbol{x}$ the eccentricity was drawn from a normal distribution with mean $\langle\varepsilon\rangle$ and standard deviation $\langle\sigma_\varepsilon\rangle$ both depending linearly on H ($\langle\varepsilon\rangle=H$, $\langle\sigma_\varepsilon\rangle=0.025H$). The $\sigma^l{}_{mn}$ were drawn from normal distributions with average values $\sigma_{ee}=\sigma_{ie}=1.9$, $\sigma_{ei}=1.4$, $\sigma_{ii}=0.6$, respectively, and identical SD equal to $0.003H$. The orientation φ of the Gaussian was drawn from a uniform distribution between 0° and 180°. All parameters were drawn independently at each location $\boldsymbol{x}$ and were, apart from the offsets $\sigma^l{}_{mn}$, identical for all four Gaussians $M_{mn}(\boldsymbol{x},\boldsymbol{y})$. Finally, each synthesized matrix m was normalized such that the real part of its principle eigenvalue was equal to 1.

To model a spontaneous event, we applied to both the excitatory and the inhibitory population an input drive

$$J_m(\mathbf{x}) = 1 + \eta\, G_m(\mathbf{x}), \qquad m \in \{e,i\} \tag{S10}$$

that was constant in time and randomly modulated across space, where G is Gaussian white noise band-pass filtered around the spatial scale Λ, which is the dominant scale of activity patterns for the homogeneous isotropic case (H=0). The realization of the Gaussian noise G was different for the excitatory and inhibitory populations. Different spontaneous events were obtained by using different realizations of input drive J_m and different initial conditions (same connectivity M). We systematically varied the input modulation strength η between 0.0004 and 0.4. All other parameters and the numerical implementation were identical to the homogeneous isotropic model described in the previous section.

We found that introducing heterogeneity into this network yielded results very similar to those reported in Fig. 4 for the one-dimensional Mexican hat model. For high values of heterogeneity H and intermediate input modulation η the heterogeneous two-population model accounts quantitatively for all aspects of the correlation structure that we observe in the early visual cortex (Extended Data Fig. 11). We thus conclude that lateral connections that are short-range but heterogeneous can produce modular patterns of activity that are correlated over an extended distance in space. The effect of heterogeneity is to induce long-range network correlations and these mechanisms appears independent from the specific form of network interactions that produce modular activity.

References

[44] Turing, AM. The Chemical Basis of Morphogenesis. Phil Trans R Soc B 237, 37–72. issn: 0962-8436 (1952).
[45] Ermentrout, GB & Cowan, JD. A mathematical theory of visual hallucination patterns. Biol Cybern 34, 137–150. issn: 03401200 (1979).
[46] Dalva, MB. Remodeling of inhibitory synaptic connections in developing ferret visual cortex. Neural Development 5. issn: 17498104. doi:10.1186/1749-8104-5-5 (2010).
[47] Chen, B, Boukamel, K, Kao, JPY & Roerig, B. Spatial distribution of inhibitory synaptic connections during development of ferret primary visual cortex. Exp Brain Res 160, 496–509. issn: 0014-4819 (2005).
[48] Levy, RB & Reyes, AD. Spatial profile of excitatory and inhibitory synaptic connectivity in mouse primary auditory cortex. J Neurosci 32, 5609–5619. issn:1529-2401 (2012).
[49] Kang, K, Shelley, M & Sompolinsky, H. Mexican hats and pinwheels in visual cortex. PNAS 100, 2848–2853. issn: 0027-8424 (2003).
[50] Ali, R, Harris, J & Ermentrout, B. Pattern formation in oscillatory media without lateral inhibition. Phys Rev E 94, 012412. issn: 24700053 (2016).
[51] Bressloff, PC, Cowan, JD, Golubitsky, M, Thomas, PJ & Wiener, MC. Geometric visual hallucinations, Euclidean symmetry and the functional architecture of striate cortex. Phil Trans R Soc B 356, 299–330. issn: 0962-8436 (2001).
[52] Cross, MC & Hohenberg, PC. Pattern-Formation Outside of Equilibrium. Rev Mod Phys 65, 851–1112. issn: 1539-0756 (1993).